metals

MDPI

Article

Effect of Natural Aging on Precipitation Strengthening Behaviors in Al-Mg-Si Alloy

Zhenjie Cui [1,2,3], Haichang Jiang [1,3,4,*], Duo Zhang [1,3], Yuanyuan Song [1,3], Desheng Yan [1,3] and Lijian Rong [1,3,*]

[1] CAS Key Laboratory of Nuclear Materials and Safety Assessment, Institute of Metal Research, Chinese Academy of Science, Shenyang 110016, China; zjcui17s@imr.ac.cn (Z.C.); dzhang15s@imr.ac.cn (D.Z.); songyuanyuan@imr.ac.cn (Y.S.); dsyan@imr.ac.cn (D.Y.)
[2] School of Materials Science and Engineering, University of Science and Technology of China, Shenyang 110016, China
[3] Shi-Changxu Innovation Center for Advanced Materials, Institute of Metal Research, Chinese Academy of Sciences, Shenyang 110016, China
[4] Shandong Key Laboratory of Advanced Aluminum Materials and Technology, Binzhou 256606, China
* Correspondence: hcjiang@imr.ac.cn (H.J.); ljrong@imr.ac.cn (L.R.)

Abstract: Natural aging (NA) is unavoidable in Al-Mg-Si alloys during actual manufacturing. Revealing the reasons for the alloy strength reduction caused by the negative NA effect is of great significance to research and practice. In this work, atom probe tomography (APT) and transmission electron microscopy (TEM) were employed simultaneously to study the effect of NA on precipitates and their contributions to the strength of Al-Mg-Si alloys. It was found that the numerous clusters formed after significant NA are unstable and will dissolve into the matrix during initial AA. However, a few stable clusters are undissolved and will result in abnormal growth of β″, which then transforms to β′. Due to the decrease of nucleation sites resulting from the abnormal growth of precipitates, more solute atoms remain in the matrix. The calculation results show that the strengthening of the solid solution atoms is much smaller than that of large-sized β′, which is much less than that of fine β″. Therefore, lengthy NA causes a significant reduction in AA strength of the Al-Mg-Si alloy.

Keywords: Al-Mg-Si alloy; natural aging; clusters; precipitates; atom probe tomography

check for updates

Citation: Cui, Z.; Jiang, H.; Zhang, D.; Song, Y.; Yan, D.; Rong, L. Effect of Natural Aging on Precipitation Strengthening Behaviors in Al-Mg-Si Alloy. *Metals* **2022**, *12*, 470. https://doi.org/10.3390/met12030470

Academic Editors: Carlos Capdevila-Montes and Martin Heilmaier

Received: 12 January 2022
Accepted: 6 February 2022
Published: 10 March 2022

Publisher's Note: MDPI stays neutral with regard to jurisdictional claims in published maps and institutional affiliations.

Copyright: © 2022 by the authors. Licensee MDPI, Basel, Switzerland. This article is an open access article distributed under the terms and conditions of the Creative Commons Attribution (CC BY) license (https://creativecommons.org/licenses/by/4.0/).

1. Introduction

Al-Mg-Si alloys, one kind of heat-treatable reinforced aluminum alloys, are widely used in the transportation industry (automobile, railway), architecture, and consumer goods industry due to their good combination of corrosion resistance and mechanical strength [1–3]. The elevated strength of the Al-Mg-Si aluminum alloys is attributed to the proper artificial aging (AA) process after solid solution treatment. The strengthening precipitates in these alloys generally occur in the following order: supersaturated solid solution (SSSS) → Solute clusters → GP zones → β″ → β′/Type A/Type B/Type C → β [4–7], and needle-shaped β″ is considered as the most effective strengthening phase in Al-Mg-Si alloy during the peak AA [8,9]. In addition, the Al-Mg-Si alloys can be stored for a long time at room temperature before the AA process due to inevitable factors in practice; this is called natural aging (NA).

Previous studies have found that NA is always detrimental to material strength, which poses the greatest challenge for the application of these alloys. Røyset et al. revealed that NA of 3600 h leads to the reduction of precipitate number density in the AA process, resulting in the decrease of the yield strength by at least 30 MPa in 6005 alloy [10]. Tao et al. proposed that NA 30 d reduces the AA peak hardness by 13 HV in an Al-1.0 wt% Mg-0.5 wt% Si alloy, which is related to appearance of large-sized β″ [11]. Tu et al. reported that the AA hardening rate was significantly slowed by NA of 14 d, since NA clusters delayed the formation of β″, leading to a drop of the peak hardness by 30 HV in the Al-0.5 at%

Mg-1.0 at% Si alloy [12]. The mechanism of negative NA effect suggests that NA clusters would be durable during initial AA, depleting the super-saturated solutes in the matrix, while not being favorable nucleation sites for further precipitates [11,13]. Furthermore, the annihilation of quenched vacancies could decelerate the solute diffusion rate, slowing the precipitation process [14].

Recently, we found that the NA also leads to the appearance of different types of AA precipitates [15]. Thus, the fractional and dimensional variation of each kind of precipitate is vital in controlling the precipitation strengthening [11,15]. However, the identification and quantitative estimation of the precipitates, such as scanning electron microscope (SEM) and transmission electron microscopy (TEM), is inappropriate for the traditional methods due to the size limitation. Several works relative to the atom probe tomography (APT) have focused on the compositions of NA clusters or precipitates during peak AA in Al-Mg-Si alloys [7,16]. However, researchers ignored the fractional and dimensional variation of precipitates in the peak-aged state with different NA. In this paper, 3DAP analysis and TEM characterization were employed simultaneously to reveal the fractional and dimensional variation of different precipitates in an artificial aging Al-Mg-Si alloy with different NA. Moreover, the strengthening contribution of different AA precipitates was further evaluated.

2. Materials and Methods

An Al-Mg-Si cast alloy with a nominal composition of Al-0.95 wt% Mg-0.8 wt% Si was prepared in this study. The ingots were homogenized at 550 °C for 10 h and further forged into a bar with a diameter of 40 mm. The aging treatments started with a solid solution treatment at 525 °C for 4 h, followed by water quenching. After the solid solution, the alloys were stored at room temperature for different times, before the 175 °C AA. It was found that the AA peak hardness of the alloy occurred after 8 h of AA. Two natural aging times of 10 min and 1440 min (24 h) were selected here, which were named as NA10 min and NA1440 min, respectively. For the 175 °C AA treated samples, NA10 min-AA and NA1440 min-AA are indicated hereafter.

The hardness measurement was carried out by a Micromet 5103 Vickers hardness tester (Struers, Denmark) at a load of 4.9 N with a loading time of 15 s. The tensile tests were performed on Dcs-10T Electronic universal testing machines (Shimadzu, Kyoto, Japan) at room temperature. Thin foils were prepared by Tenupol-5-type twin-jet (Struers, Denmark) electropolishing in a 30% methanol solution of nitric acid, and TEM observations were performed on JEM 2100F (Japan Electronics Co., Ltd., Tokyo, Japan). The APT samples of NA were prepared by electrolytic polishing for 10–15 min. The APT experiments were carried out on LEAP 5000 XR (Cameca Instruments, Ins, Madison, WI, USA) with laser mode at a temperature of 25 K and a laser pulse frequency of 200 kHz. The 3D reconstruction and analysis were performed using IVAS 3.8.2 software (Cameca Instruments, Ins, Madison, WI, USA). It is proven that the effect of NA can be ignored in the APT test once the preparation is completed [17]. Furthermore, the thermal analysis was carried out on Q1000 DSC (TA Instruments, New Castle, PA, USA), and the heating rate was set as 10 °C/min.

3. Results and Discussion

3.1. The Negative Effect of NA on the Alloy Strength

The NA and AA hardness curves of the Al-Mg-Si alloy drawn by averaging seven hardness indentation data are shown in Figure 1a. In the NA sample, the hardness increases fast within 300 min but tends to become stable with an increase in NA time. As previously reported, the NA hardness of the alloy increases with the continuous formation of clusters during NA [18]. When the number density of clusters reaches saturation, the peak of NA hardness of the alloy is produced [19]. On the contrary, the AA hardness decreases quickly and then keeps stable with increasing NA time. It is clear that NA shows a severe negative effect on the AA hardness of the alloy. Samples of NA10 min, NA1440 min, NA10 min-AA and NA1440 min-AA, indicated by the black arrows in Figure 1a, were selected for further

investigation. The engineering stress–strain curves of NA10 min-AA and NA1440 min-AA are presented in Figure 1b. The yield strengths of NA10 min-AA and NA1440 min-AA were 280 MPa and 230 MPa, respectively. Therefore, NA1440 min-AA lost about 18% strength compared to NA10 min-AA, indicating a severe loss of strength caused by the NA process.

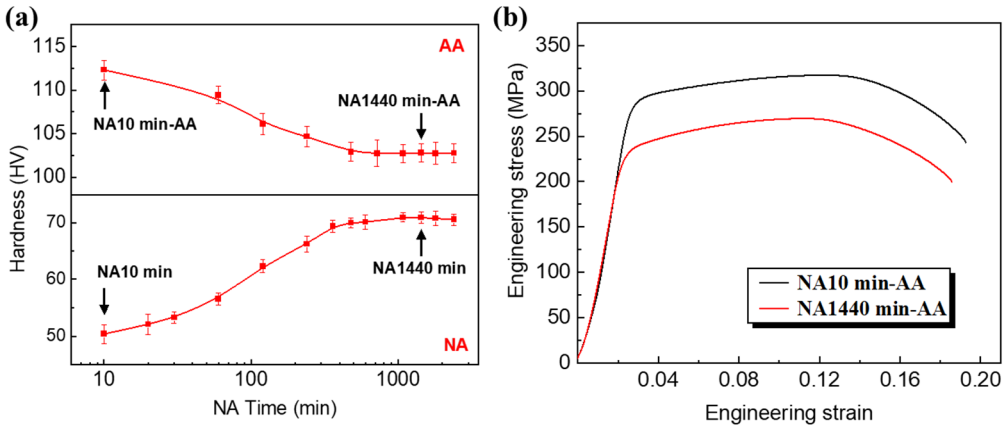


Figure 1. (**a**) NA and AA hardness curves of the Al-Mg-Si alloy. (**b**) Engineering stress–strain curves of NA10 min-AA and NA1440 min-AA.

3.2. The Influence of NA on Clusters

Figure 2a–c show the 3 NN distribution of the experimental and randomized data of Mg and Si in NA10 min and NA1440 min. No aggregation of Mg and Si solute atoms are observed in NA10 min samples, since little deviation of curves in Mg and Si are observed. However, the experimental curve significantly shifts to the right of random curve in the NA1440 min sample, illustrating the formation of Mg + Si clusters. Figure 2d,e further depicts the 3D atom maps of Mg (red) and Si (purple) of NA10 min, indicating the homogeneous distribution of solute atoms at this condition. The Mg + Si clusters of NA1440 min are also shown in Figure 2f, which is consistent with the results above. Therefore, the formation of NA clusters in NA1440 min is an important reason for the degradation of AA strength. It is commonly believed that the formation of NA clusters consumes the super-saturated solutes in the matrix but cannot provide favorable nucleation sites for other precipitates [13,20]. Instead, clusters that form at early AA are believed to be the prior nucleus for β″ [11].

After nucleation, the growth of AA precipitates the need to reach the critical size and be thermally stable in the subsequent AA process. The thermodynamic analysis was conducted for further research, and the DSC flow curves of NA10 min and NA1440 min are shown in Figure 3. The exothermic peak at 50–100 °C corresponding to the formation of clusters 2 during initial AA can be the nucleation sites of β″ [21,22]. The trough at 200–250 °C can be related to the dissolution of unstable clusters 1, formed during NA [23,24]. The peak around 250 °C and 300 °C are normally associated with the formation of β″ and β′, respectively [21,23]. NA1440 min has no exothermic peak of clusters 2. Considering the APT results in Figure 2, it can be concluded that the NA1440 min forms many clusters 1, consuming many solute atoms; hence, it does not have enough driving force to precipitate clusters 2 during initial AA. The trough of NA1440 min at 200–250 °C caused by the dissolution of clusters 1 delayed the precipitation process of precipitates, leading to the peak of β″ moving toward a higher temperature.

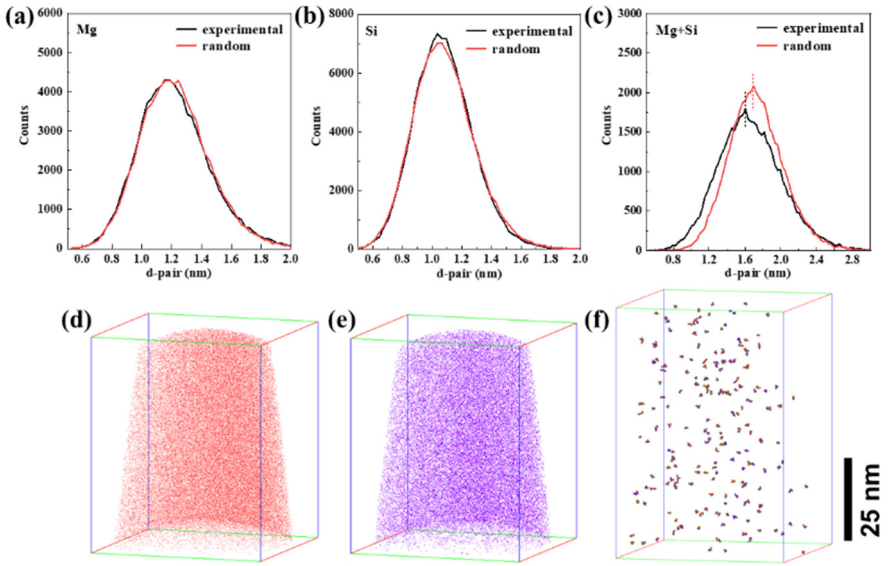


Figure 2. The 3 NN distribution of experimental and randomized data of NA10 min (**a**,**b**) and NA1440 min (**c**); And the 3D atom maps of Mg (**d**) and Si (**e**) of NA10 min and Mg + Si clusters of NA1440 min (**f**).

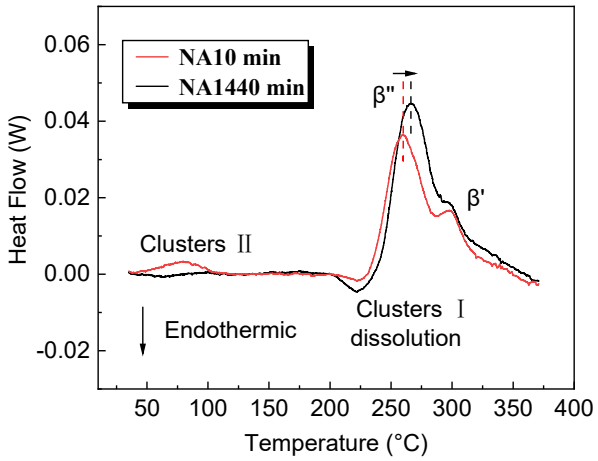


Figure 3. DSC flow curves of the Al-Mg-Si alloy at NA10 min and NA1440 min.

3.3. The Influence of NA on Precipitates

3.3.1. TEM Images

The TEM bright-field images of NA10 min-AA and NA1440 min-AA with the electron beam parallel along the <001>Al are shown in Figure 4a,b. The HRTEM images and FFTs of NA10 min-AA and NA1440 min-AA viewed along with the <001>Al are shown in Figure 4c,d. The NA10 min-AA has a fine and uniform distribution of the precipitates, as shown in Figure 4a. The length of precipitates of NA1440 min-AA becomes longer, and a few considerably elongated precipitates even exceed 200 nm. However, the number density of precipitates is significantly reduced. The FFT in Figure 4c agrees well with the monoclinic β″ [9]. Figure 4d shows the FFT of the considerably elongated precipitates, which is consistent with hexagonal β′ [25]. β″ and β′ coexist in NA1440 min-AA. The measurements of average radius (R) of β″ and β′ and the other detailed data are further estimated based on the micrographs through Image Pro Plus software, and the results are shown in Table 1. The R of β″ is 1.93 nm in NA10 min-AA, while it is 2.15 nm in NA1440 min-AA. The R of β′ is 3.23 nm in NA1440 min-AA. With the extension of NA, β″ gets coarser, and large-sized β′ appears. The abnormal growth of precipitates leads to a reduction in the number of solute atoms for nucleation, resulting in a decrease in the number of nucleation sites, which eventually leads to a decline of alloy strength.

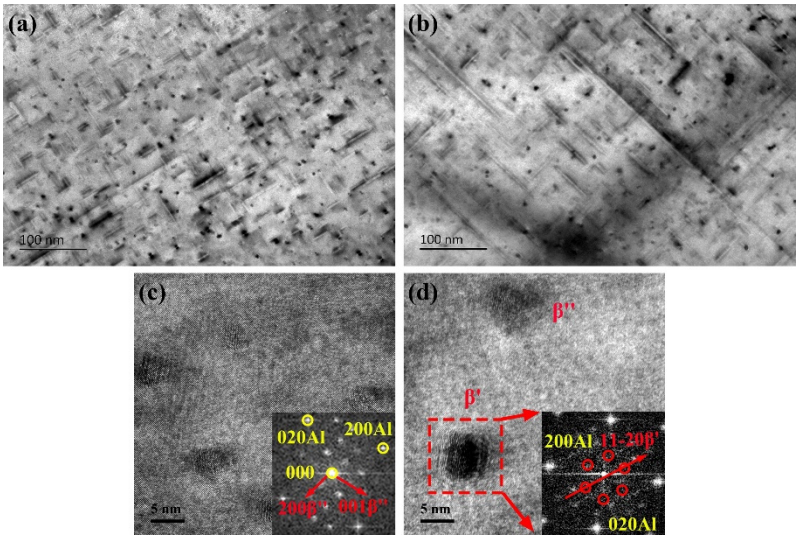


Figure 4. TEM bright-field images of (**a**) NA10 min-AA and (**b**) NA1440 min-AA. HRTEM images and FFTs of the β″ and β′ of (**c**) NA10 min-AA and (**d**) NA1440 min-AA; the images were taken with the electron beam along the <001>Al orientation.

Table 1. The relative data of precipitates in NA10 min and NA1440 min.

Samples	Precipitates	R/nm	V_f [1]	Solute in Matrix [1]
NA10 min-AA	GC	0.82 ± 0.13 [1]	0.02%	0.45 wt% Mg 0.26 wt% Si
	β″	1.93 ± 0.16 [2]	0.74%	
	Sum	-	0.76%	
NA1440 min-AA	GC	0.43 ± 0.08 [1]	0.07%	0.61 wt% Mg 0.35 wt% Si
	β″	2.15 ± 0.11 [2]	0.14%	
	β′	3.23 ± 0.27 [2]	0.16%	
	Sum	-	0.37%	

[1] Parameters determined from the APT data. [2] Average radius R of β″ and β′ are shown in the bright-field images in Figure 4.

3.3.2. APT Maps

The 3D atom maps of Mg (Orange), Si (purple), and a 10.0 at% Mg + Si iso-concentration surface of NA10 min-AA and NA1440 min-AA are shown in Figure 5a,b. The precipitates in the NA1440 min-AA are more coarse and reduced in number density compared with NA10 min-AA, which is consistent with the TEM results in Figure 4. The inter-particle spacing of precipitates in NA10 min-AA is small; that is, the nucleation sites of β″ are close to each other. In addition, the precipitates in NA1440 min-AA are sparsely distributed. Additionally, APT can obtain the composition of the precipitates. Figure 5c,d demonstrates the 1D concentration profiles of representative β″ and β′, marked in yellow in Figure 5a,b, respectively. The 1D concentration profiles, which were measured by a selected cylinder with a moving step of 0.3 nm, distinguished β″ and β′ in terms of their compositions. The Mg/Si ratio of β″ and β′ are 0.83 and 1.84, and the content of Al is 32.13 at% and 19.22 at%, respectively. This indicates that the transformation process from β″ to β′ is dominated by Mg, and Al is continuously discharged, which is consistent with Ref. [10].

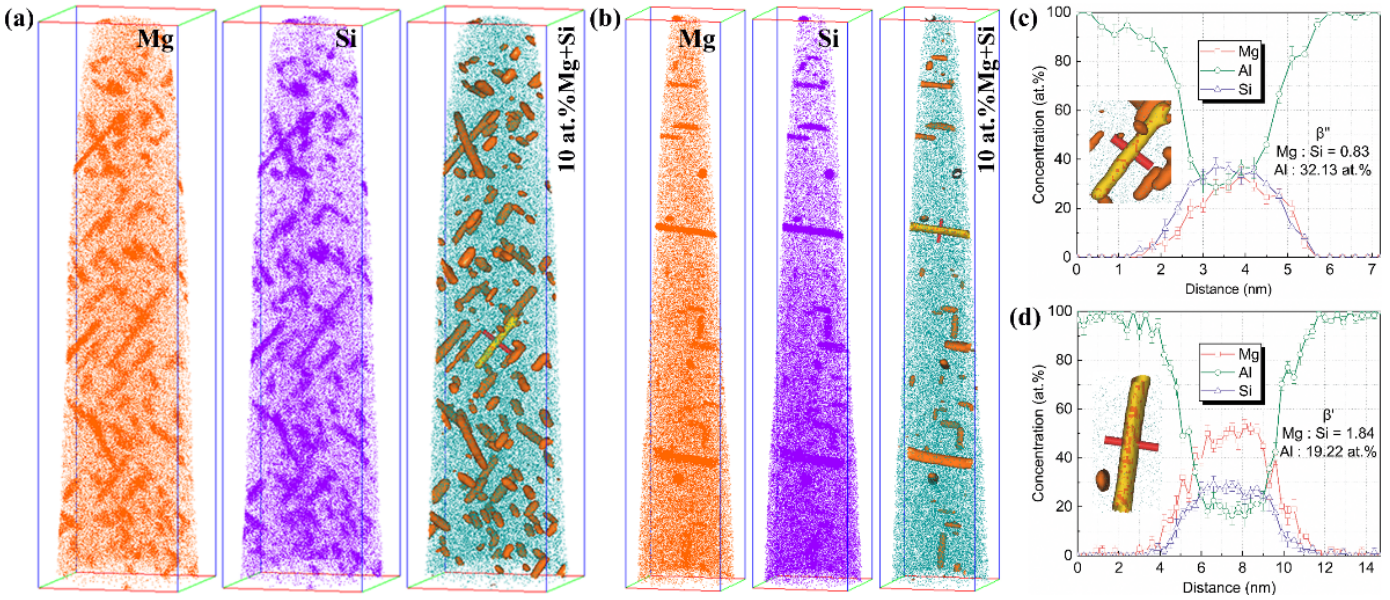


Figure 5. The 3D atom maps of Mg, Si, and a 10.0 at% Mg + Si iso-concentration surface of (**a**) NA10 min-AA (86 nm × 90 nm × 260 nm) and (**b**) NA1440 min-AA (82 nm × 82 nm × 480 nm); Al(Green), Mg(Orange), and Si(purple). The representative 1D concentration distribution of (**c**) β″ and (**d**) β′ is marked in yellow in Figure 4a,b, respectively.

3.4. Size and Volume Fractions of Precipitates

The maximum separation method is applied to distinguish the various precipitates of NA10 min-AA and NA1440 min-AA according to previous studies, with d_{max} = 0.7 nm and N_{min} = 10 [15,26]. Detailed information on differentiating different precipitates is provided in the Supplementary Materials, and all the statistical data of different precipitates are listed in Table 1. The clusters and GP zones at the AA state are collectively referred to as spherical precipitates, abbreviated as GC. It is considered that the supersaturation of the solute and the presence of vacancies are necessary for nucleation of GC during AA in small local regions of the Al lattice between the large precipitates [27]. The volume fraction of GC increases with the extending of NA time. A low fraction of GC in NA10 min-AA can be attributed to greater consumption of the solute by densely distributed β″, with a volume fraction of 0.74%. The β″ and β′ become coarser in NA1440 min-AA, and the overall volume fraction drops to 0.37%, including 0.14% β″ and 0.16% β′. Additionally, it can be obtained from the 'Solute in matrix' that more solute atoms remain in the matrix at NA1440 min. This is probably because the numerous NA clusters deplete the supersaturated solutes, reducing the driving force of precipitation. The solute atoms thus remain in the matrix during AA.

3.5. The Contribution from Different Precipitates to the Alloy Strength

Separation of the contribution from different types of precipitates to the alloy strength is calculated in this section. Previous studies [28,29] have reported that precipitates with a cross-section radii larger than 7.5 nm were bypassed by dislocations, while those with a cross-section radii smaller than 7.5 nm were sheared by dislocations. Therefore, the dislocation shear mechanism is used in precipitation strengthening calculations in this paper. The yield strength σ_y of the Al-Mg-Si alloys consists of precipitation hardening σ_p, solid solution strengthening σ_s, and lattice resistance σ_i. The overall yield strength calculation can be achieved by adding the various contributions, as in Equation (1) [18,29–31]. The σ_p can be explained mainly from the modulus strengthening σ_{mod}, chemical strengthening σ_{chem}, coherence strengthening σ_{coh}, and σ_{GC}, which is the contribution from GC, as shown in Equation (2) [29,30,32,33].

$$\sigma_y = \sigma_p + \sigma_s + \sigma_i \quad (1)$$

$$\sigma_p = \sigma_{cut} = \sigma_{mod} + \sigma_{chem} + \sigma_{coh} + \sigma_{GC} \quad (2)$$

Detailed information of equations and parameters for calculation is provided in the Supplementary Materials. Inputting the data from Table 1 and Table S1, the calculation results of the various contributions of precipitates are shown in Table 2. For the NA10 min-AA sample, the yield strength is mainly derived from $\sigma_{\beta''}$, which is 221 MPa. For the NA1440 min-AA sample, β′ with a volume fraction of 0.16% contributes 54 MPa to the yield strength, while 0.14% β″ contributes 101 MPa. This fully demonstrates that β″ is the main strengthening phase in Al-Mg-Si alloy and the appearance of large-sized β′ is a major cause of the negative NA effect. σ_y' is the yield strength obtained by the tensile test, as shown in Figure 1b. σ_y' is similar to the calculation results, which proves that the selection of the calculation formula is reasonable. Importantly, the relationship between strength and the size and volume fraction of precipitates is not linear, which shows that the comparison of strength increments per unit volume fraction at different states is not meaningful.

Table 2. The calculation results of the various contributions of precipitates.

Strength (MPa)		NA10 min-AA	NA1440 min-AA
$\sigma_{\beta''}$	σ_{mod}	14.6	6.5
	σ_{chem}	0.7	0.3
	σ_{coh}	206.1	94.6
	Sum	221	101
$\sigma_{\beta'}$	σ_{mod}	-	13.3
	σ_{chem}		0.7
	σ_{coh}		40.1
	Sum		54
σ_{GC}		2.3	4.2
σ_s		44.0	53.8
σ_i		10.0	10.0
σ_y		277	223
σ_y'		280	230

3.6. Reasons for the Occurance of Lower Strength in the NA1440 min-AA Sample

Figure 6 demonstrates the typical atom maps, showing the distribution of Al, Mg, and Si atoms in NA10 min-AA and NA1440 min-AA, in which the coexistence of GC, β″, and β′ can be clearly observed. The GC is marked in blue, β″ is depicted in black, and β′ in yellow. At NA10 min-AA, the nucleation sites are close to each other; β″ developed at the same time, with no abnormal growth. At NA1440 min-AA, the precipitates are sparsely distributed, and regions marked as A around β′ are comparatively Al-rich and Mg- and Si-poor compared with other regions. At NA1440 min-AA, from the beginning of AA, unstable NA clusters dissolve into the matrix, and when the solute supersaturation in the matrix meets the nucleation satisfaction, the formation of stable clusters and the dissolution of unstable clusters occur simultaneously. With the extending AA time, abnormal growth of a few β″ occurs on the stable clusters, which is then converted to β′. This abnormal growth process makes it easier to capture the surrounding solute atoms, forming the solute atoms' poor region A, which directly restricts the growth of the GC. Additionally, the solute atoms in region B, for which there is no nucleation site, do not have enough driving force to diffuse and precipitate, but they stay in the matrix. This is one of the reasons for the significant decrease of the volume fraction of the precipitates in the NA1440 min-AA.

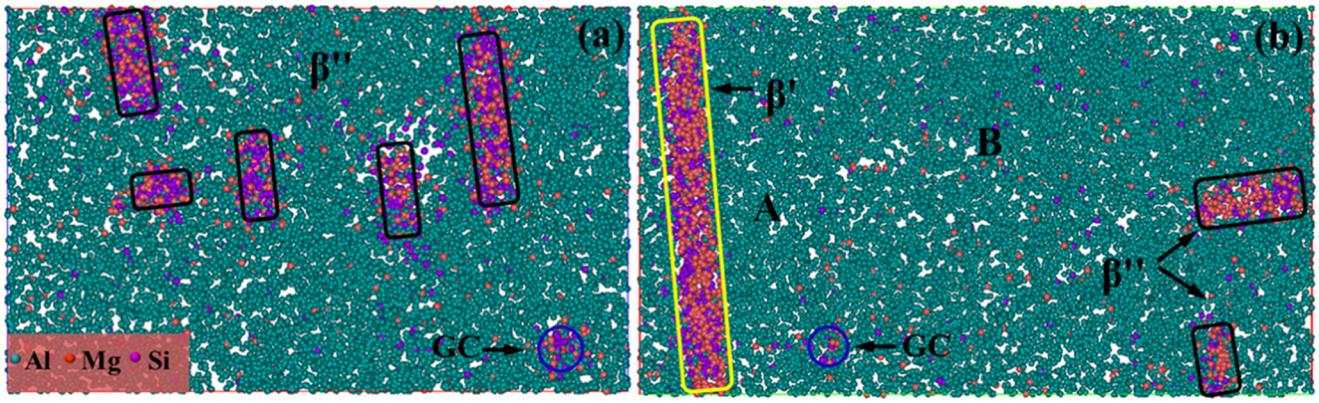


Figure 6. Typical 1 nm thick atom maps, showing the distribution of Al, Mg, and Si atoms at (**a**) NA10 min-AA (65 nm × 40 nm) and (**b**) NA1440 min-AA (70 nm × 40 nm).

Based on the above discussion, the AA process of short NA and long NA are summarized through the schematic diagram in Figure 7. Solute atoms of short NA are evenly distributed. During initial AA, sufficient solute atoms quickly precipitate a large number of stable clusters, which act as nucleation sites to form fine and dense β″ during the peaking AA. Long NA formed numerous unstable clusters, which dissolve into the matrix during initial AA. A longer time is needed to dissolve the unstable clusters, and only when the solute supersaturation in the matrix reaches the nucleation condition, the formation of nucleation sites can occur. Under this condition, the distance between nucleation sites is usually very large. With the extending AA time, abnormal growth of β″ on the few nucleation sites occurs, which is then transformed to β′. The surrounding solute atoms are more easily captured in this abnormal growth process, which directly restricts the growth of the GC. Additionally, the abnormal growth of the precipitates also leads to the decrease of nucleation sites, so that more solute atoms remain in the matrix. The strengthening of the solid solution atoms is much smaller than that of the coarse β′, and coarse β′ is much smaller than that of fine β″. This is the fundamental reason for the significant decrease in the strength of alloy with long-time NA.

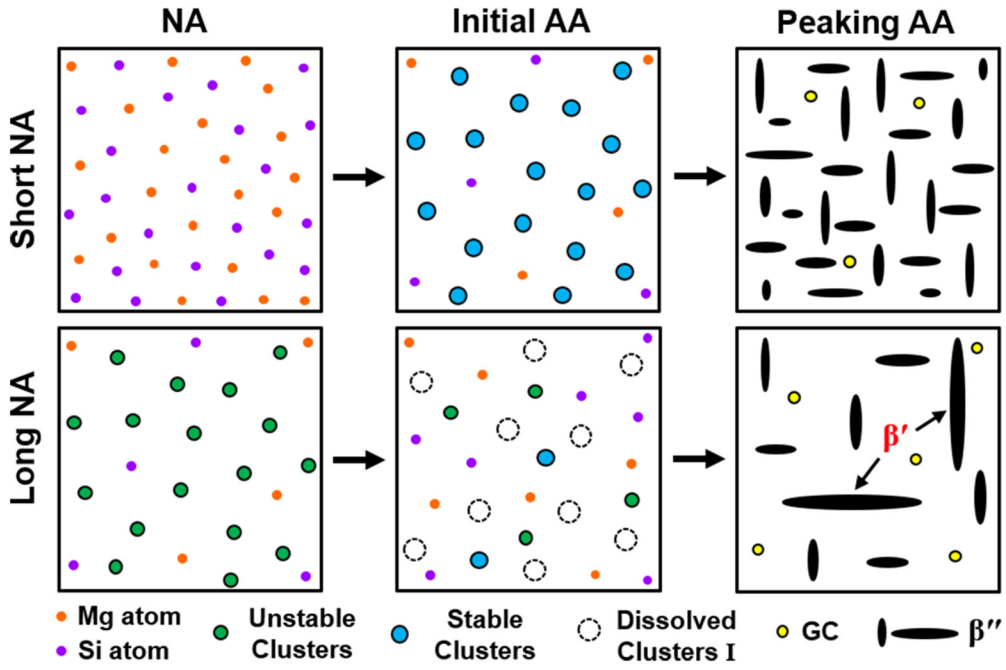


Figure 7. The schematic diagram of the AA process of short NA and long NA.

4. Conclusions

(1) Separation of the contribution from different types of precipitates to the alloy strength was evaluated in this work. At the NA10 min-AA, the yield strength is mainly derived from $\sigma_{\beta''}$ which is 221 MPa. At the NA1440 min-AA, β′ with a volume fraction of 0.16% contribute 54 MPa to the yield strength, while 0.14% β″ contributes 101 MPa. This fully demonstrates that β″ is the main strengthening phase in Al-Mg-Si alloy, and the appearance of large-sized β′ is a major cause of the decreased strength.

(2) Growth of the GP zone and clusters between β′ during AA can be restrained because the surrounding solute atoms are more easily captured by large-sized β′. Therefore, such a GP zone and clusters will be wrapped by more Al atoms, which explains the survival of a greater GP zone and more clusters in NA1440 min-AA.

(3) The nature of the clusters during NA is considered to be responsible for the reduced strength of the alloy after AA. Owing to the instability of NA clusters and reduction in nucleation driving force, the nucleation sites are decreased, so that more solute atoms remain in the matrix. The strengthening of the solid solution atoms is much smaller than that of the large-sized β′, and large-sized β′ is much smaller than that of fine β″. This is the fundamental reason for the significant decrease in the strength of NA1440 min-AA.

Supplementary Materials: The following supporting information can be downloaded at: https://www.mdpi.com/article/10.3390/met12030470/s1, Table S1: The relative data of precipitates in the different states; Table S2: The parameters used in the calculation [15,18,26,28–35].

Author Contributions: Z.C.: methodology, investigation, formal analysis, data curation, writing—original draft preparation; H.J.: review and editing, supervision, funding acquisition; D.Z.: methodology, software; Y.S.: resources, methodology, review and editing; D.Y.: resources; L.R.: review and editing, supervision, funding acquisition. All authors have read and agreed to the published version of the manuscript.

Funding: This research was funded by the National Key R&D Program of China (Grant No. 2016YFB1200602), the Strategic Priority Program of the Chinese Academy of Sciences (Grant No. XDB22020000), and Shenyang Key R&D and technology transfer program (Grant No. Z19-1-004).

Data Availability Statement: The data presented in this study are available on request from the corresponding author. The data are not publicly available due to an ongoing study.

Conflicts of Interest: The authors declare no conflict of interest.

References

1. Li, H.; Mao, Q.Z.; Wang, Z.X.; Miao, F.F.; Fang, B.J.; Song, R.G.; Zheng, Z. Simultaneously enhancing the tensile properties and intergranular corrosion resistance of Al–Mg–Si–Cu alloys by a thermo-mechanical treatment. *Mat. Sci. Eng. A Struct.* **2014**, *617*, 165–174. [CrossRef]
2. Kumar, N.; Goel, S.; Jayaganthan, R.; Brokmeier, H.G. Effect of grain boundary misorientaton, deformation temperature and AlFeMnSi-phase on fatigue life of 6082 Al alloy. *Mater. Charact.* **2017**, *124*, 229–240. [CrossRef]
3. Guo, M.X.; Du, J.Q.; Zheng, C.H.; Zhang, J.S.; Zhuang, L.Z. Influence of Zn contents on precipitation and corrosion of Al-Mg-Si-Cu-Zn alloys for automotive applications. *J. Alloy Compd.* **2019**, *778*, 256–270. [CrossRef]
4. Ding, L.; Jia, Z.H.; Nie, J.F.; Weng, Y.Y.; Cao, L.F.; Chen, H.W.; Wu, X.Z.; Liu, Q. The structural and compositional evolution of precipitates in Al-Mg-Si-Cu alloy. *Acta Mater.* **2018**, *145*, 437–450. [CrossRef]
5. Edwards, G.A.; Stiller, K.; Dunlop, G.L.; Couper, M.J. The precipitation sequence in Al-Mg-Si alloys. *Acta Mater.* **1998**, *46*, 3893–3904. [CrossRef]
6. Andersen, S.J.; Marioara, C.D.; Friis, J.; Wenner, S.; Holmestad, R. Precipitates in aluminium alloys. *Adv. Phys. X* **2018**, *3*. [CrossRef]
7. Buchanan, K.; Colas, K.; Ribis, J.; Lopez, A.; Garnier, J. Analysis of the metastable precipitates in peak-hardness aged Al-Mg-Si(-Cu) alloys with differing Si contents. *Acta Mater.* **2017**, *132*, 209–221. [CrossRef]
8. Andersen, S.J.; Marioara, C.D.; Vissers, R.; Froseth, A.; Zhandbergen, H.W. The structural relation between precipitates in Al-Mg-Si alloys, the Al-matrix and diamond silicon, with emphasis on the trigonal phase U1-$MgAl_2Si_2$. *Mat. Sci. Eng. A Struct.* **2007**, *444*, 157–169. [CrossRef]

9. Yang, W.; Wang, M.P.; Zhang, R.R.; Zhang, Q.; Sheng, X.F. The diffraction patterns from β″ precipitates in 12 orientations in Al-Mg-Si alloy. *Scripta Mater.* **2010**, *62*, 705–708. [CrossRef]
10. Royset, J.; Stenne, T.; Sater, J.A.; Reiso, O. The effect of intermediate storage temperature and time on the age hardening response of Al-Mg-Si alloys. *Mater. Sci. Forum* **2006**, *519–521*, 239–244. [CrossRef]
11. Tao, G.H.; Liu, C.H.; Chen, J.H.; Lai, Y.X.; Ma, P.P.; Liu, L.M. The influence of Mg/Si ratio on the negative natural aging effect in Al–Mg–Si–Cu alloys. *Mat. Sci. Eng. A Struct.* **2015**, *642*, 241–248. [CrossRef]
12. Tu, W.B.; Tang, J.G.; Ye, L.Y.; Cao, L.F.; Zeng, Y.; Zhu, Q.Q.; Zhang, Y.; Liu, S.D.; Ma, L.H.; Lu, J.K.; et al. Effect of the natural aging time on the age-hardening response and precipitation behavior of the Al-0.4Mg-1.0Si-(Sn) alloy. *Mater. Design* **2021**, *198*, 109307. [CrossRef]
13. Aruga, Y.; Kozuka, M.; Takaki, Y.; Sato, T. Formation and reversion of clusters during natural aging and subsequent artificial aging in an Al-Mg-Si alloy. *Mat. Sci. Eng. A Struct.* **2015**, *631*, 86–96. [CrossRef]
14. Zurob, H.S.; Seyedrezai, H. A model for the growth of solute clusters based on vacancy trapping. *Scripta Mater.* **2009**, *61*, 141–144. [CrossRef]
15. Cui, Z.J.; Jiang, H.C.; Zhang, D.; Song, Y.Y.; Yan, D.S.; Rong, L.J. Influence of Mn on the negative natural aging effect in 6082 Al alloy. *Mat. Sci. Eng. A Struct.* **2020**, *793*, 139874. [CrossRef]
16. Cao, L.; Rometsch, P.A.; Couper, M.J. Clustering behaviour in an Al–Mg–Si–Cu alloy during natural ageing and subsequent under-ageing. *Mat. Sci. Eng. A Struct.* **2013**, *559*, 257–261. [CrossRef]
17. Dumitraschkewitz, P.; Uggowitzer, P.J.; Gerstl, S.S.A.; Loffler, J.F.; Pogatscher, S. Size-dependent diffusion controls natural aging in aluminium alloys. *Nat. Commun.* **2019**, *10*. [CrossRef]
18. Starink, M.J.; Cao, L.F.; Rometsch, P.A. A model for the thermodynamics of and strengthening due to co-clusters in Al–Mg–Si-based alloys. *Acta Mater.* **2012**, *60*, 4194–4207. [CrossRef]
19. Seyedrezai, H.; Grebennikov, D.; Mascher, P.; Zurob, H.S. Study of the early stages of clustering in Al-Mg-Si alloys using the electrical resistivity measurements. *Mat. Sci. Eng. A Struct.* **2009**, *525*, 186–191. [CrossRef]
20. Madanat, M.; Liu, M.; Banhart, J. Reversion of natural ageing in Al-Mg-Si alloys. *Acta Mater.* **2018**, *159*, 163–172. [CrossRef]
21. Chang, C.S.T.; Banhart, J. Low-Temperature Differential Scanning Calorimetry of an Al-Mg-Si Alloy. *Metall. Mater. Trans. A* **2011**, *42*, 1960–1964. [CrossRef]
22. Noseda Grau, V.; Cuniberti, A.; Tolley, A.; Castro Riglos, V.; Stipcich, M. Solute clustering behavior between 293 K and 373 K in a 6082 Aluminum alloy. *J. Alloy Compd.* **2016**, *684*, 481–487. [CrossRef]
23. Gupta, A.K.; Lloyd, D.J.; Court, S.A. Precipitation hardening in Al-Mg-Si alloys with and without excess Si. *Mat. Sci. Eng. A Struct.* **2001**, *316*, 11–17. [CrossRef]
24. Zhang, Z.; Xu, H.H.; Wu, S.N.; Liu, Y. Effects of combined pre-straining and pre-aging on natural aging and bake hardening response of an Al-Mg-Si alloy. *Acta Metall. Sin Engl.* **2013**, *26*, 340–344. [CrossRef]
25. Vissers, R.; Van Huis, M.A.; Jansen, J.; Zandbergen, H.W.; Marioara, C.D.; Andersen, S.J. The crystal structure of the β′ phase in Al-Mg-Si alloys. *Acta Mater.* **2007**, *55*, 3815–3823. [CrossRef]
26. Sha, G.; Moller, H.; Stumpf, W.E.; Xia, J.H.; Govender, G.; Ringer, S.P. Solute nanostructures and their strengthening effects in Al–7Si–0.6Mg alloy F357. *Acta Mater.* **2012**, *60*, 692–701. [CrossRef]
27. Buha, J.; Lumley, R.N.; Crosky, A.G. Precipitation and solute distribution in an interrupted-aged Al–Mg–Si–Cu alloy. *Philos. Mag.* **2008**, *88*, 373–390. [CrossRef]
28. Teichmann, K.; Marioara, C.D.; Andersen, S.J.; Marthinsen, K. TEM study of β′ precipitate interaction mechanisms with dislocations and β′ interfaces with the aluminium matrix in Al-Mg-Si alloys. *Mater Charact.* **2013**, *75*, 1–7. [CrossRef]
29. Yang, M.; Chen, H.N.; Orekhov, A.; Lu, Q.; Lan, X.Y.; Li, K.; Zhang, S.Y.; Song, M.; Kong, Y.; Schryvers, D.; et al. Quantified contribution of β″ and β′ precipitates to the strengthening of an aged Al-Mg-Si alloy. *Mat. Sci. Eng. A Struct.* **2020**, *774*, 138776. [CrossRef]
30. Esmaeili, S.; Lloyd, D.J.; Poole, W.J. Modeling of precipitation hardening for the naturally aged Al-Mg-Si-Cu alloy AA6111. *Acta Mater.* **2003**, *51*, 3467–3481. [CrossRef]
31. Marceau, R.K.W.; Vaucorbeil, A.; Sha, G.; Ringer, S.P.; Poole, W.J. Analysis of strengthening in AA6111 during the early stages of aging: Atom probe tomography and yield stress modelling. *Acta Mater.* **2013**, *61*, 7285–7303. [CrossRef]
32. Ardell, A.J. Precipitation Hardening. *Metall. Trans. A* **1985**, *16A*, 1985–2131. [CrossRef]
33. Song, M. Modeling the hardness and yield strength evolutions of aluminum alloy with rod/needle-shaped precipitates. *Mat. Sci. Eng. A Struct.* **2007**, *443*, 172–177. [CrossRef]
34. Guo, M.X.; Du, J.Q.; Zheng, C.H.; Zhang, J.S.; Zhuang, L.Z. Solute clustering in Al-Mg-Si-Cu-(Zn) alloys during aging. *J. Alloy. Compd.* **2019**, *774*, 347–363. [CrossRef]
35. Myhr, O.R.; Grong, Ø.; Andersen, S.J. Modelling of the age hardening behaviour of Al–Mg–Si alloys. *Acta Mater.* **2001**, *49*, 65–75. [CrossRef]